DOI: 10.13009/EUCASS2019-360

Numerical Investigation of a Resonance Ignition System

Christian BAUER, Paul LUNGU and Oskar J. HAIDN
Institute for Turbomachinery and Flight Propulsion, Rocket Propulsion Group
Technical University of Munich, Boltzmannstr. 15, 85748 Garching
christian.bauer@ltf.mw.tum.de, paul.lungu@ltf.mw.tum.de, haidn@tum.de

Abstract

This study uses the commercial CFD solver Ansys Fluent to numerically reproduce experimental results of a resonance ignition system operated with gaseous methane and oxygen. It highlights the advantages and drawbacks of the used models and attempts to map the operating envelope of the igniter. By simulating the transient heat-up of the igniter, possible design improvements are identified. Additionally, the importance of turbulence in predicting the useful igniter operating range is highlighted.

Nomenclature

JRM	Jet Regurgitant Mode	d_{th}	Injector throat diameter
JSM	Jet Screech Mode	d	Injector outlet diameter
NPR	Nozzle pressure ratio	D_1	Resonator cavity inlet diameter
τ	Characteristic time	D_2	Resonator cavity tip diameter
k	Heat Conductivity	D_{torch}	Ignitor outlet throat diameter
c_p	Heat capacity at const. pressure	L	Resonator cavity length
h	Heat transfer coefficient	ξ	Characteristic length
ϵ	Emissivity	Δt	Timestip width
f_0	Fundamental frequency	ϑ	Non-dimensional time, t/τ_{conv}
v	Speed of sound	G_k	Production of Turb. Kinetic Energy
X	Axial coordinate	C_{lim}	TKE production limiter factor
s	Nozzle-resonator distance		

1. Introduction

The importance of a reliable ignition system for rocket propulsion can hardly be overstated, and for decades the available methods of ignition have influenced the design of rocket combustion chambers and even entire stages. The widespread use of hydrazine and its derivates can at least partly be attributed to its ease of ignition, which requires only a suitable catalyst or the presence of a compatible oxidizer. Some kerosene/LOX based engines like Saturn-V's F-1 or SpaceX's Merlin mimic this behaviour through the injection of pyrophoric mixtures during engine start-up. However, the resulting high probability of ignition comes at a price, even when toxic and carcinogenic properties are neglected.

The high reactivity of these substances makes strict adherence to operating procedures a must, and numerous incidents during the long history of hydrazine-use show, that the handling of hypergolic propellants leaves little to no margin for human error [1]. This was dramatically highlighted in the Damascus Titan Missile Incident, in which a small propellant leak, caused by a dropped tool, led to the accidental launch of a nuclear warhead [2]. But also the pyrophoric TEA/TEB mixture currently used by SpaceX requires careful handling, as shown by the launch abort caused by oxygen pollution of the igniter feed lines [3]. This approach of using hypergolic substances to ignite the engine provides high reliability and potentially the ability to re-ignite during flight. Re-Ignitability is also advertised for the upcoming Ariane 6 upper stage engine Vinci as a big advantage, which is claimed to give the flexibility to carry out missions not possible with the current launcher [4]. In contrast to the SpaceX approach, the Vinci igniter uses a conventional spark torch igniter fed from dedicated high-pressure tanks [5]. However, both approaches have the severe drawback of introducing an additional, constrained resource into the system, and in fact the loss of one Falcon 9 core stage can be attributed to running out of TEA/TEB [6].

Both applications could potentially benefit from resonance ignition, which uses Hartmann-Sprenger resonators to passively heat up propellants beyond their auto-ignition temperature, without the need for movable parts or electrical

DOI: 10.13009/EUCASS2019-360

systems. From a system point of view this makes the propellants quasi-hypergolic and thus provides all the benefits of classical hypergolic substances, but without their undesirable side-effects.

Hartmann-Sprenger Tubes are the devices that initiate and maintain gas oscillations that drive passive heating through non-reversible processes and are thus the basis for all types of resonance ignition systems. During Pitot-probe measurements of underxpanded free-stream jets Hartmann observed strong pressure oscillations in these probes, which were accompanied by very high sound pressure levels of more than 150 db [7] [8]. Sprenger later discovered, that under certain conditions large SPLs are also accompanied by high temperatures in the resonating gas [9]. Both macroscopically observable effects are aspects of the same physical principle and several useful applications are obvious for both. However, despite considerable effort no conclusive explanation exists to date of how the fluid oscillations are generated and maintained. This may also explain, why the same arrangement of a nozzle directing a free-stream jet towards a cavity closed on one end is known under different names: Powered Resonance Tube, Hartmann-Sprenger Tube, Hartmann-Whistle, Air-Jet Generator and more, all describe the same experimental arrangement.

One of the challenges of finding a conclusive description of the mode of operation is the fact, that the flow in Hartmann-Sprenger Tubes is strongly influenced by many variables: resonator geometry, nozzle-resonator spacing, nozzle pressure ratio and gas species have all been shown to exert considerable influence on the flow. This has led to the situation, that many experimental results seem to contradict each other. Sarohia and Back were able to clear some of the confusion by identifying distinct oscillation modes, which allowed classifying and ordering the wealth of experimental results [10]. Of the three operating modes they identified, only two are relevant to the current application.

In the Jet Regurgitant Mode, which mostly occurs when the resonator opening is located in the vicinity of the Mach Discs of the free jet, the flow cycle can be divided into distinct phases. During the inflow phase, the free-stream enters and fills the resonator cavity. Often this flow is accompanied by a series of relatively weak compression waves, which can coalescent into a single shock, if the cavity is long enough. At the closed end the shock may be reflected, brings the fluid in the cavity to rest and travels upstream towards the resonator opening, where it is then reflected as expansion wave. This initiates the next flow phase. If the compression by the preceding shock was strong enough, the fluid then exits the cavity in the form of an underexpanded free jet, which pushes the opposing jet emanating from the nozzle upstream until the pressure in the resonator has decreased so far that the outflow stops and a new flow cycle begins. These cycles occur in the order of the first acoustic longitudinal mode of the cavity, but due thermal gradients and other non-linear effects the actual frequency is hard to predict. It is worth noting that under certain conditions the pressure in the resonator cavity can easily surpass the total nozzle supply pressure and fall below ambient pressure.

When NPR and s/d values are not well matched, Jet Screech Mode can occur, which is characterized by oscillation frequencies much higher than those of the JRM. Under these conditions, often a bow shock in front of the cavity can be observed which vibrates in axial direction and induces numerous but weak compression waves travelling into the resonator. Since the fluid inside the cavity is nearly at rest, the mass exchange between the free jet and the cavity is strongly reduced.

Sarohia et al observed strong thermal effects when resonators with high length-to-diameter ratios operated in the JRM and when low L/d-cavities oscillated in the JSM. Consequently, knowing which operating mode can be expected under given boundary conditions is a must, if a reliable resonance ignition system is to be designed. The large number of influencing variables makes it difficult to systematically screen large parameter spaces experimentally. Therefore, numerical methods may provide help in pre-selecting promising candidate configurations.

Previous studies could predict the experimental heating rates and auto-ignition at individual load points sufficiently well to warrant further investigation [11]. However, numerical studies that attempt to predict the mode of operation are very limited and only investigate the acoustic effects [12]. To date not a single study is known that systematically investigates the attainable heating rates over larger parameter ranges. This may be attributed to the fact, that most studies are carried out using explicit methods, which allow capturing moving shocks with great detail. However, the timescales associated with resonant heating are typically much larger than those of the convective processes, which makes these schemes prohibitively expensive for this kind of application. Additionally, due to the low thermal power of the resonant heating process the gas temperature is highly sensitive to heat losses to the surrounding resonator material. Consequently, tight coupling of fluid and solid walls is required to solve the conjugated heat transfer problem with sufficient accuracy. In this study a solution strategy is presented, which may be used to analyse and predict the performance of resonance ignition systems. This is a vital step in deriving improved designs.

2. Test Case Description

In previous studies a 30 kW resonance igniter operated with methane and oxygen showed good reliability under both nominal and off-design operation [11, 13]. However, a scaled down version with a TDP of 12 kW for application in a

DOI: 10.13009/EUCASS2019-360

500 N thruster failed to reliably ignite the propellants, despite producing high gas temperatures during resonant heating [14]. Lungu attributed this to insufficient propellant mixing inside the resonator cavity and therefore changed the inlet nozzle from a coaxial design with separate inlets for methane and oxygen to a single, convergent-divergent geometry for premixed fluids. This premixed nozzle design is numerically investigated in the current work and the data from his experiments serve as basis for validating the calculations. Details on the igniter design and the experimental results can be found in [14], but a brief description is also given here.

The overall igniter design is depicted in Figure 1. In order to start the passive heating process, oxygen is introduced through the injector (2,3), where it forms a free jet and impinges on the resonator cavity (4). When all necessary conditions are satisfied a strong interaction between the free jet and the cavity occurs, which leads to violent oscillations in the cavity. Since a part of the fluid remains in the cavity and undergoes repeated compression and expansion, irreversible effects gradually lead to increased temperatures in this region. When the heating is considered sufficient, additional methane is introduced into the igniter through the same inlet nozzle. When encountering the pre-heated, high-temperature oxygen in the cavity, it ignites. The resulting flame then travels towards the open end of the cavity, anchors there and propagates until it exits the igniter through the outlet nozzle.

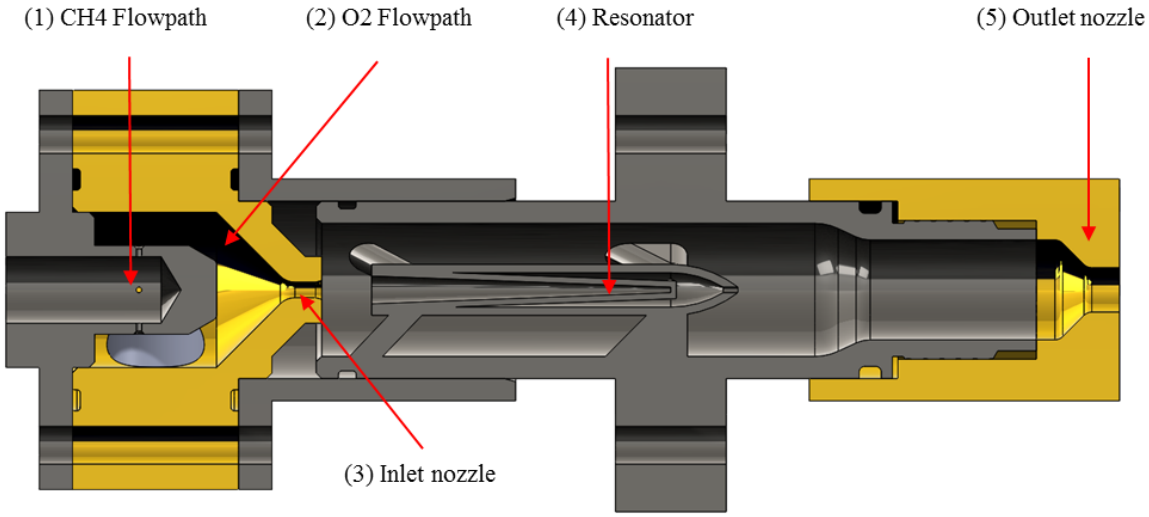

Figure 1: Modular igniter design consisting mainly of injector assembly (1-3), resonator (4) and outlet (5).

Due to the dimensioning of the injector and outlet throat diameters, both cross sections are choked during the heat-up phase, and thus the ratio between injector and ignitor pressure (NPR) is fixed. While Lungu investigated various NPR regimes, this work only considers a single NPR of ≈ 8.3. An overview over the most important design parameters are summarized in Table 1.

Table 1: Igniter design parameters

d_{th}	1.4 mm	NPR	8.3
d	1.7 mm	TDP	12 kW
D_1/d	≈1.5	$\dot{m}_{O_2}$	7.2 g/s
D_{torch}/d_{th}	2.86	p_{O_2}	1.8 MPa
D_1/D_2	5	O/F	30
L/D_1	10.8		

3. Discussion of Solvers and Models

The investigations presented in this paper were conducted with the commercial, general-purpose CFD solver Ansys Fluent v182. It transforms time-dependent, compressible RANS equations into algebraic form by finite-volume discretization. In order to compute the flux-balance over these control volumes, the values at the face centres have to be reconstructed from the values stored at the centre of the volume.

For diffusive terms a simple 2nd order central differencing scheme is used. Convective terms, however, usually require special treatment in order to maintain solution stability. In the context of this work convective fluxes are obtained

DOI: 10.13009/EUCASS2019-360

through a form of the QUICK scheme, which is a formally 3rd order hybrid scheme, using a weighted blending of a 2nd order upwind and a central differencing scheme. The classical QUICK scheme is known to produce only small oscillations with low penetration depths downstream of discontinuities [15]. In contrast to the conventional QUICK scheme with a fixed weighting of central and upwind terms, the implementation in Fluent claims to use a solution-adaptive weighting to maintain monotony and the effective order of the method depends on the flow field [16].

Time-dependant terms can be discretized with the 1st or 2nd order Backward Euler scheme. For the pressure-based solver, also a bounded version of the 2nd order Euler scheme is available, which introduces additional bounding factors. While the exact nature of these is not documented, their general form suggests that they may introduce some monotony-preserving temporal limiting. For gradient reconstruction from cell-centered values the Green-Gauß Node Based method is used, which may reduce checkerboarding effects in structured meshes by taking the values of diagonal cell neighbours into account.

Since the flow in Hartmann-Sprenger Tubes can experience severe discontinuities, a compromise between excessive solution limiting and unphysical oscillations has to be found. From the three limiter formulations available in Fluent, the Differential Limiter is used, which is based on the work of Venkatakrishnan [17] with solution-adaptive extensions proposed by Wang [18]. An additional Limiter Filter is used to relax the monotony-preserving condition in smooth flow regions, but no details are provided on their implementation.

For the pressure-based solver, a coupled formulation is used, which constructs a monolithic system of equations from all flow variables, which is solved iteratively. Due to the importance of pressure in this system, special schemes are used for pressure reconstruction. Despite the importance of this reconstruction, the solver documentation provides surprisingly little information in this regard. The bodyforce-weighted method has been empirically determined to provide the best results for Hartmann-Sprenger type of flows.

Evaluating the face mass fluxes in the continuity equation requires reconstructing the face normal velocity from cell-centered values. Fluent uses the work of Rhie/Chow [19] to obtain these values and uses momentum-weighted averaging of the coefficients in the continuity equation to introduce the necessary pressure-velocity coupling. Further information on this averaging function, however, is not provided by the solver documentation. The resulting system of equations is solved iteratively by an Algebraic Multigrid Solver. Since the density-based solver, also available in Fluent, did not provide stable solutions for all investigated load points, this work presents results obtained with the pressure-based solver.

The effects of turbulence are approximated with the Realizable $k-\epsilon$ (RKE) model, which is based on the work of Shih et al [20]. It ensures realizability (and thus avoids negative Reynolds shear stresses) by replacing a constant in the standard $k-\epsilon$ (SKE) model with a solution adaptive value, which takes the mean strain rate into account. Shih also derived a new formulation for the epsilon equation based on the dynamic equation for the mean-square vorticity fluctuations. Both enhancements help to remedy the Round Jet Anomaly of the SKE and improve the model performance for round freestream jets.

Since this model uses the Boussinesq approximation, it uses additional turbulence production limiters to dampen the excessive production of turbulence kinetic energy near stagnation points [21, 22]. These are of the form:

$$\dot{k} = \min(G_k, C_{lim}\rho\epsilon) \quad \textbf{(1)}$$

where G_k is the production of turbulence kinetic energy prior to limiting, and C_{lim} a constant clipping factor. Preparatory investigations on HSTs showed, that this limiter can disturb the onset of large-scale oscillations in the flow and can severely alter the viscous heating in the resonator. For a larger resonator configuration, a limiter clipping factor of 400 was empirically determined to yield acceptable results. However, it will be shown that for the present study a value around 10 is more appropriate. This suggests, that more extensive fine-tuning of the underlying turbulence models is necessary, which is however beyond the scope of this work.

4. Timescales

Simulation of a conjugate heat transfer problem can be challenging since convective and conductive timescales are usually on different orders of magnitude. According to Wolf [23] and Marin [24] the timescale of a conduction problem can be estimated from:

DOI: 10.13009/EUCASS2019-360

$$\tau_{cond} = \alpha \xi^2 \quad \textbf{(2)}$$

where ξ represents a characteristic length and α the thermal diffusivity of the material.

For the EOS MP1 CoCrMo powder temperature-dependant heat conductivity and a density of $\rho = 8300[kg/m^3]$ are specified in the data sheet for this material [25]. For the specific heat capacity temperature-dependant values are estimated from ASTM F75, which has nearly the same chemical composition [26, 27]. Using the resonator wall thickness as the characteristic dimension and the diffusivity at a mean temperature of ≈500 K results in a conductive timescale of $\tau_{cond} \approx 54ms$.

This is orders of magnitude larger than those of the driving convective processes, which can be characterized by the fundamental frequency of the employed resonator cavity. Based on linear acoustic theory the eigenfrequency f_0 of a conical cavity is given by [28]:

$$\frac{2\pi f_0}{v} L = \pi - tan^{-1}\left(\frac{2\pi f_0}{v} x\right) \quad \textbf{(3)}$$

Here the factor x denominates the truncated length of a virtual, full cone, v the temperature-dependent speed of sound and L the cavity length. For a mean temperature of 650 K this results in a fundamental frequency of ≈6075 Hz and a characteristic timescale of $\tau_{conv} \approx 0.165ms$. However, this theoretical value is considerably larger than that derived from the experimentally measured frequency of ≈4600 Hz. Instead, the current resonator appears to behave more like a cylindrical $\lambda/4$ resonator with additional end-correction:

$$f_{0,cyl} = \frac{v}{4(L + 0.4D)} \quad \textbf{(4)}$$

Equations (3) and (4) are depicted in Figure 2 for a mean fluid temperature between 200 and 1000 K. It can be seen, that the presented conical resonator matches the fundamental frequency of a cylindrical cavity with a mean oxygen temperature of about 800 K better than that of a conical cavity.

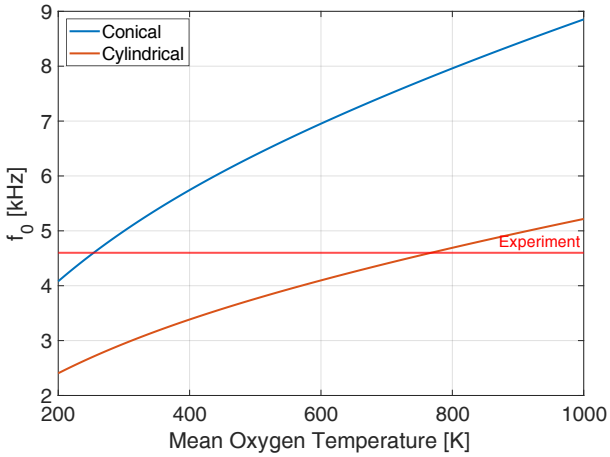

Figure 2: Fundamental frequencies for conical and cylindrical cavities, compared to experimental data.

From this comparison it can be deduced, that linear acoustic theory is not sufficient to describe the oscillations occurring in Hartmann-Sprenger Tubes.

With the experimentally determined convective timescale of $\tau_{conv} = 0.22\ ms$ the ratio of conductive to convective timescale amounts to:

$$R_{\tau,physical} = \frac{\tau_{cond}}{\tau_{conv}} \approx 250 \quad \textbf{(5)}$$

In order to artificially reduce this ratio and thus speed up the calculation, different timesteps sizes in fluid (Δt_{fluid}) and solid (Δt_{solid}) regions can be employed.

DOI: 10.13009/EUCASS2019-360

$$R_{\tau,sim} = \frac{1}{R_{\Delta t,Sim}} \frac{\tau_{cond}}{\tau_{conv}} = \frac{\Delta t_{fluid}}{\Delta t_{solid}} \frac{\tau_{cond}}{\tau_{conv}} \quad \textbf{(6)}$$

By specifying a solid-to-fluid timestep ratio of $R_{\Delta t,Sim} > 1$ the numerical timescale ratio can be reduced, which speeds up the convergence to the quasi-steady limit cycle. Depending on the goal of the simulation, various values for the numerical timescale ratio $R_{\tau,sim}$ are desirable: if the quasi-steady limit cycle is of interest, values around unity can be used to minimize calculation times. However, this also eliminates the thermal averaging and lowpass effect of the solid. If the transient thermocouple measurements are to be reproduced, larger values should be used, at the expense of additional computation time. In this work a ratio of solid to fluid timestep size of $R_{\Delta t,Sim} \approx 150$ is used, which is considered an acceptable compromise between computational effort and accuracy.

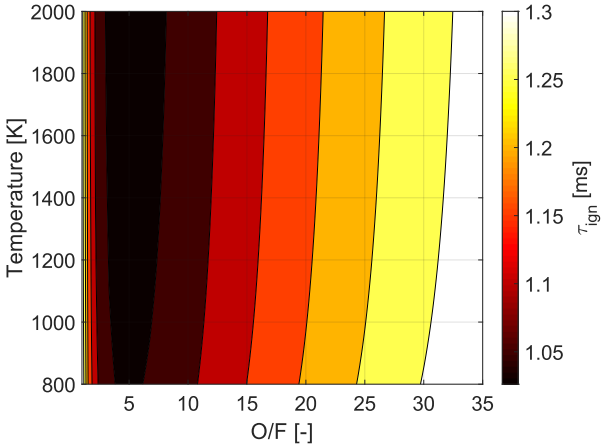

Figure 3: Auto-ignition delay of methane/oxygen mixtures at 0.4 MPa.

The investigated resonance igniter is designed to operate with methane and oxygen, which exhibit considerably larger auto-ignition delays compared to hydrogen-oxygen-systems. Zhang et al investigated this delay for methane-oxygen mixtures and obtained a relation [29], which is visualized in Figure 3. This shows, that the chemical timescales are at least in the same order as those describing convective effects. Employing finite-rate chemistry is therefore a must, and strong coupling between chemistry and turbulence should also be taken into account.

5. Calculation Domain and Mesh

The calculation domain used in the current investigation, shown in Figure 4, includes not only the essential nozzle, cavity and torch fluid, but also incorporates the solid material of the resonator itself, as well as a small fluid region between the inner resonator cone and the surrounding shroud. Since the maximum temperature of the resonating fluid is strongly affected by heat losses, this shroud is designed to shield the inner resonator cone from convective heat losses. For manufacturing reasons, the shroud is open at the tip and therefore the deadwater region between inner cone and shroud is connected to the ambient fluid through a small fluid channel. Due to strong pressure oscillations in the entire igniter, fluid may enter and exit this region repeatedly, which may increase the convective heat losses and thus reduce igniter temperature. By including both solid and deadwater zone, this effect can be estimated in the present work.

By including the solid in the same solver complete two-way coupling of the conjugated heat transfer problem is achieved. This is important, because earlier studies have shown that the heat generated in the resonator cavity is comparatively low, and thus gas temperature is also influenced by the temperature of the surrounding solid [11]. Since the walls between solid and fluid are fully coupled the boundary conditions of the simulation problem are rather simple and consist of a mass flow inlet, pressure outlet, adiabatic walls and an axis. Because the torch outlet is choked, the downstream pressure was slightly reduced below experimentally measured values to avoid separation and recirculation in the diverging part of the outlet nozzle, which improves convergence in these areas slightly without affecting the flow upstream of the throat. The parameters for all boundary conditions are summarized in Table 2.

DOI: 10.13009/EUCASS2019-360

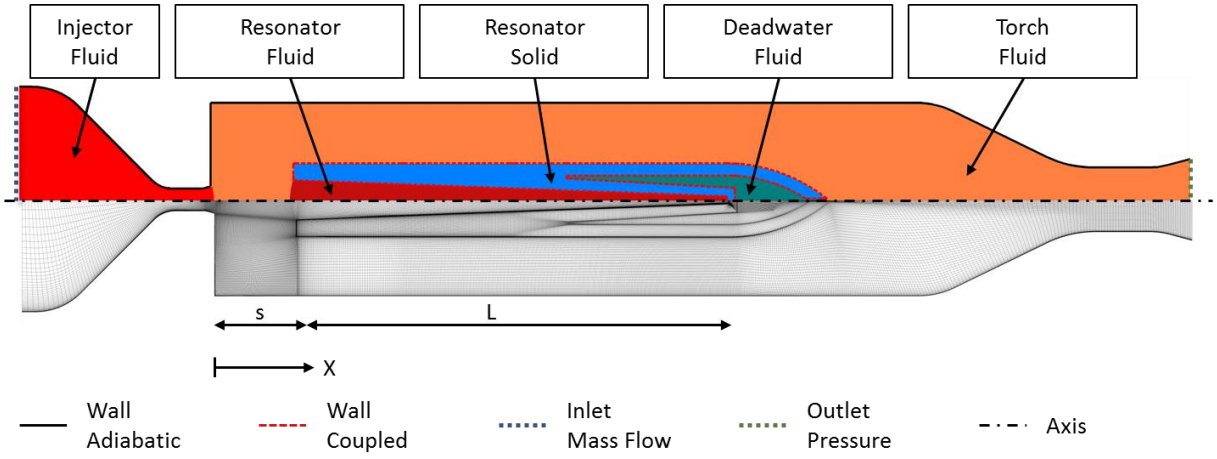

Figure 4: Calculation domain and fully conformal hex mesh for a refinement factor of 75%

Table 2: Boundary conditions for fully coupled case

Symbol	Type	Parameter
·····	Mass Flow Inlet	$\dot{m} = 7.1\frac{g}{s}$, $T = 282K$, $p \approx 1.8MPa$, $I_t = 5\ \%$, $\mu_t/\mu = 10$
·····	Pressure Outlet	$T = 282K$, $p = 900kPa$, $I_t = 5\ \%$, $\mu_t/\mu = 10$
——	Adiabatic Wall	$h = 0\,W/m^2K$, $K_s = 0\,\mu m$
- - - - -	Coupled Wall	$K_s = 0\,\mu m$
- · - ·	Axis	-

Since the boundary layers in the nozzle and the resonator cavity are of importance, the mesh is adapted to yield a maximum value of $y^+ \approx 1$ and the low-Re Menter-Lechner Wall Treatment is employed. The required wall resolution was determined empirically by simulating a single flow cycle. However, since the flow in the cavity repeatedly reverses direction or comes to rest, y^+ values are considerably below unity for most of the time. It is worth noting, that the reversing flow also leads to situations, where the flow in the boundary layer is faster or in the opposite direction to the core flow.

While solving the heat conduction equation in the solid region itself is not computationally expensive, it indirectly increases the cost by leading to slower convergence in the fluid cells adjacent to the solid wall. This is considered a weakness in the implementation of the used solver and can partly be compensated by fine-tuning grid partitioning. For some investigations, however, wall temperatures are only of secondary interest. In these instances, the solid and deadwater region can be removed from the domain and a simplified thin-wall model may be employed to account for heat losses. In this thermal-resistance type of model heat capacity is neglected and inner and outer walls are separated by a virtual wall of constant thickness. When the thin-wall model is employed, the first halve of the cavity wall closer to the injector nozzle is considered isothermal, while the second halve near the tip is modelled as diabatic. There the outer wall convective heat transfer coefficient is estimated from free convection around a cylinder with a diameter of 0.58 mm and a temperature of 650 K [30]. The emissivity is estimated as 0.4, which is close to the value specified for uncharred Inconel at elevated temperatures [31]. A summary of these boundary conditions can be found in Table 3.

DOI: 10.13009/EUCASS2019-360

Table 3: Summary of resonator wall boundary conditions for thin-wall model

$(\mathbf{X}-\mathbf{s})/\mathbf{L}$	$\mathbf{t}[\mathbf{mm}]$	$\mathbf{h}[\mathbf{W}/(\mathbf{m}^2\ \mathbf{K})]$	$\mathbf{T}_\infty[\mathbf{K}]$	$\boldsymbol{\epsilon}[-]$
0-25%	1.17	∞	282	-
25-50%	1.43	∞	282	-
50-75%	0.72	24	282	0.4
75-100%	0.61	24	282	0.4
100% (tip)	0.5	24	282	0.4

6. Discretization and Convergence

Ideally, the flow field should be independent of numerical resolution in time and space. However, with respect to typical CFD meshes, shock discontinuities are infinitely thin and can therefore not be completely resolved. Additionally, despite built-in measures to suppress spurious oscillations near shocks, some degree of oscillation still occurs.

This sensitivity can be quantified with a least-squares version of the Grid Convergence Index (GCI), which estimates the resolution-dependent error for different meshes from a solution extrapolated to a theoretical, infinitely fine mesh [32, 33]. By applying safety factors to the error estimation, depending on the apparent order of convergence, error bars for the 95 % confidence interval can be obtained.

In this study the mesh is parameterized, which allows for the structured and uniform refinement necessary to obtain meaningful results from the GCI algorithm. Additionally, the domain geometry can be changed parametrically, and the mesh adapts to these changes by maintaining a constant node density. By starting from a reference mesh and varying the number of nodes in each direction by a factor of 50 to 175 %, more than one order of change in number of cells is investigated.

The data for the mesh and timestep study was obtained from transient simulations employing the thin-wall model. After $t = 1.5\tau_{conv}$ flow properties at the axis are analysed at selected points. These sample points were determined by a peak-search algorithm, in order to focus on areas with large gradients where the strongest sensitivity to discretization occurs. In smooth areas, where no peaks occur over longer distances, additional sample points were inserted between the peaks.

The resulting GCI analysis can be seen in Figure 5 for the mesh with a refinement factor of 100 %. For comparison, this analysis was performed for both the pressure-based (left) and density-based solver (right). It can be seen, that the estimated error in most parts of the domain is small, except in regions with strong gradients. There, the density-based solver fares considerably better than the pressure-based formulation, as the latter tends to produce spurious oscillations downstream of the pressure waves in the resonator around X/d=8 and X/d=16. These oscillations could be traced back to the Rhie-Chow p-v-coupling and are virtually independent of the spacial discretization methods.

The oscillations upstream of the injector outlet are remnants of pressure waves, which are originally generated by the intentionally unphysical step function pressure initialization and are reflected back and forth inside the injector plenum. These are not relevant to production-run simulations and can therefore be safely ignored.

DOI: 10.13009/EUCASS2019-360

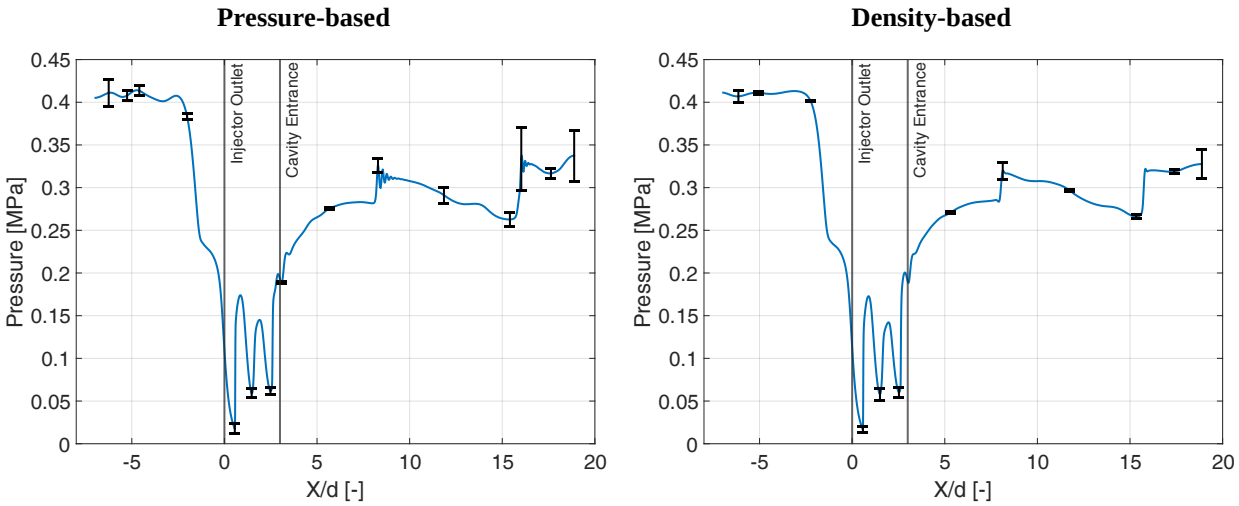

Figure 5: Instantaneous axial pressure distribution for the pressure-based (top left) and density-based (top right) solver on mesh with 100 % refinement after $1.5\tau_{conv}$. Error bars (below) obtained via a least-squares version of GCI, indicating the 95 % confidence range for pressures at selected X/d ratios.

The difference between both solvers can be seen more clearly in Figure 6, which directly compares the axis pressures throughout the domain (left), as well as in the narrow area around the upstream travelling pressure wave near X/d=8 (right). Both solvers capture the location of the pressure wave correctly, but while the density-based formulation produces only a single over- and undershoot up- and downstream of the front, the pressure-based solver experiences multiple oscillations downstream of the wave front. These spurious oscillations do not seem to negatively affect the flow farther downstream of the wave front, but the exact contribution of this excess variation to viscous heating after several flow cycles has yet to be established.

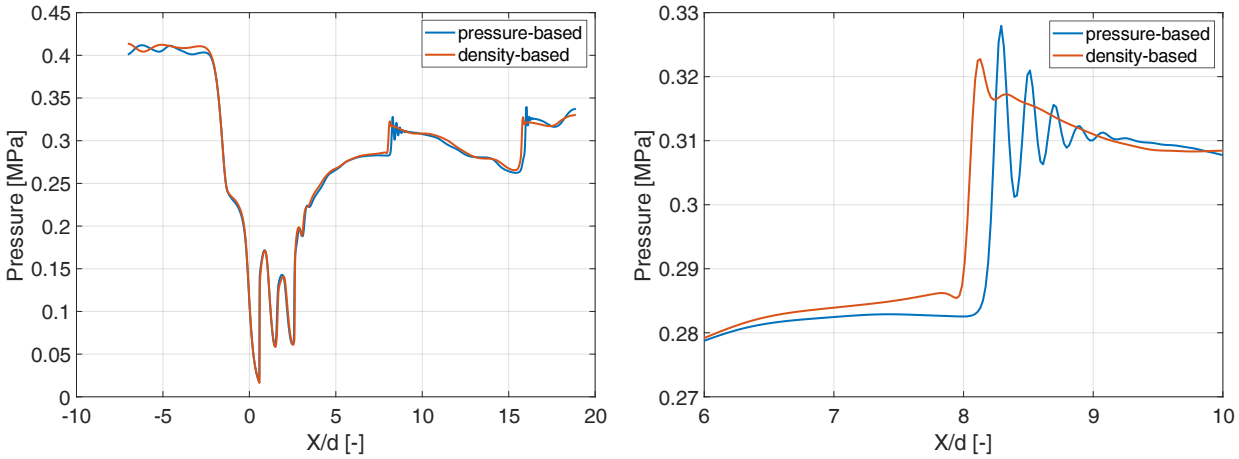

Figure 6: Axial pressure distribution for the pressure and density-based implicit solver on mesh with 150 % refinement after $1.5\tau_{conv}$. The right plot shows the details of the discontinuity closest to the nozzle, around X/d=8.

The development of the pressure value at some of the more critical locations over the mesh refinement factor can be seen in Figure 7 for both solvers. The larger error bars for the pressure-based solver (left) are driven mainly by the large deviation of the coarsest mesh, compared to the density-based solver (right). Generally, the values change little for meshes with a refinement exceeding 100 %. Consequently, a mesh refinement of 100 % is used for the remaining part of this work.

DOI: 10.13009/EUCASS2019-360

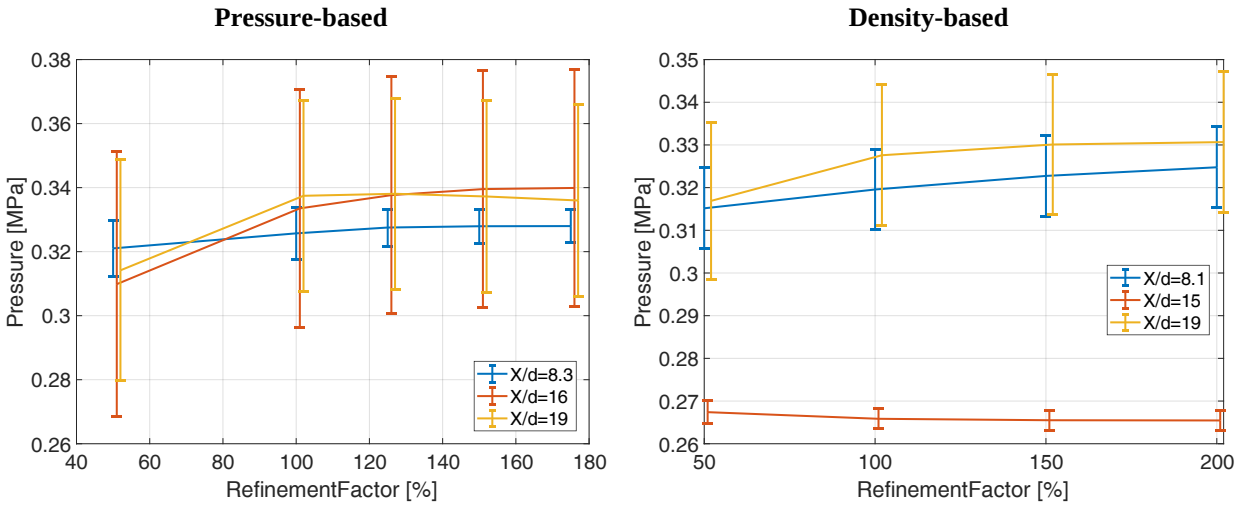

Figure 7: Pressure at selected peaks over mesh refinement factor and the corresponding GCI error bars for both pressure-based (left) and density-based solver (right).

The error bars in Figure 5 show that most parts of the flow are remarkable insensitive to mesh refinement, which can be attributed to the 3rd order discretization in smooth flow areas. Mesh refinement mainly affects the spurious oscillations following pressure front and thus the pressure-based solver is more affected by changing spacial resolution.

Above mesh sensitivity study was performed with a fixed timestep size of 50 ns. However, the reproduction of small flow features depends not only on spacial, but also on temporal discretization. Even though GCI was developed for quantifying uncertainty regarding mesh resolution, it can also be used for characterizing the influence of timestep size variation.

Figure 8 presents the results of a temporal GCI analysis on a mesh with 100 % refinement at timestep sizes of 20, 50 and 100 ns. Normalized with the experimentally determined convective timescale of $\tau_{conv} = (4kHz)^{-1}$ this translates to about 2500, 5000 and 12500 timesteps per flow cycle.

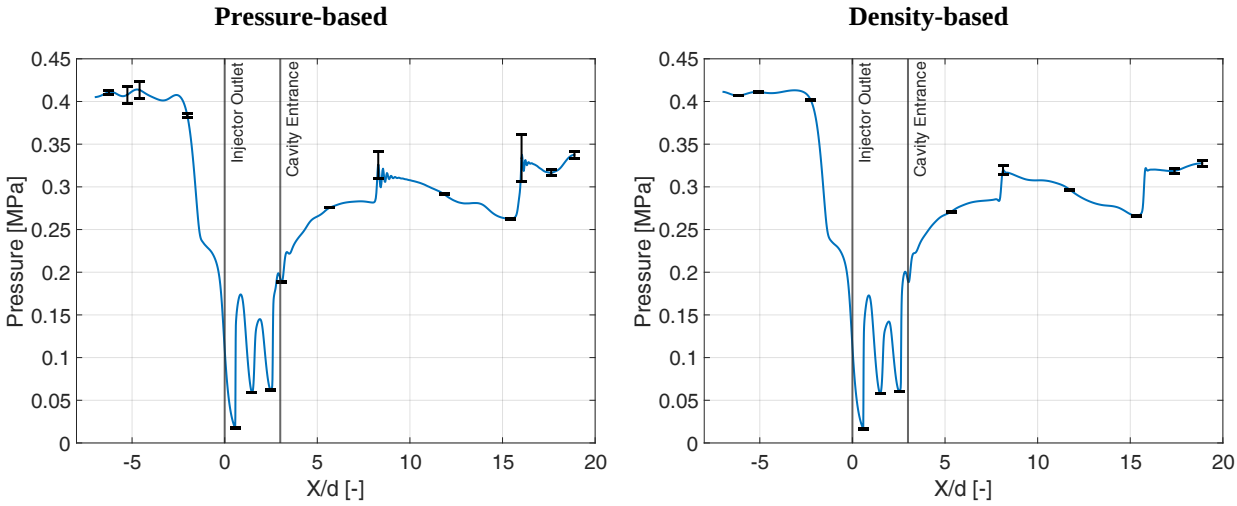

Figure 8: Instantaneous axial pressure distribution for the pressure-based (top left) and density-based (top right) solver on mesh with 100 % refinement after $1.5\tau_{conv}$. Error bars are obtained via GCI algorithm for timestep sizes of 20, 50 and 100 ns and plotted for $\Delta t = 50ns$.

The error bars indicate, that for most parts of the flow this time resolution is more than sufficient to capture all relevant phenomena, even for the largest timestep. However, the pressure fronts in the pressure-based formulation are affected more severely. This can be seen more clearly in the left part of Figure 9, which shows the axis pressure around the first pressure wave front for different timestep sizes. Reducing the timestep width helps to steepen the wave front, but it also increases the amplitude and special frequency of the spurious oscillations. This means, that further reducing the timestep size may not necessarily provide more accurate results. For the remainder of this work a timestep size of 50 ns (or 5000 timesteps/flow cycle) is used.

DOI: 10.13009/EUCASS2019-360

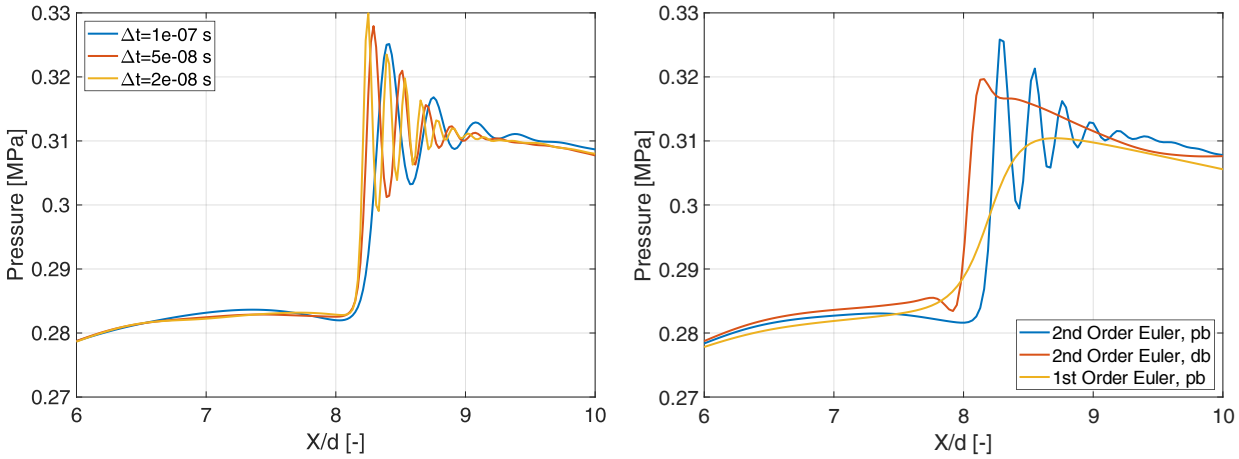

Figure 9: Left: Axial pressure distribution around the pressure front around X/d=8 for the pressure-based solver and a mesh refinement of 100 % for different timestep sizes. Right: Comparison of the same region for density-based solver and different discretization orders for the pressure-based formulation.

The analysis in this section shows, that for the present application the density-based Roe-FDS scheme is clearly superior to the Rhie-Chow scheme of the pressure-based solver. It is therefore very unfortunate, that the density-based solver experiences stability issues for most of the relevant igniter load points. These issues mainly occur through divergence of the k-equation and are more pronounced for the $k-\epsilon$ turbulence model than for the SST.

As shown by the right part of Figure 9 it is possible to eliminate the spurious oscillations of the Rhie-Chow-Scheme by employing first order time discretization. This comes at the price of a considerable blurring of the wave front, which can only be compensated by reducing the timestep size extensively. A small reduction in oscillation amplitude can also be achieved by switching off higher-order terms of the Rhie-Chow scheme through unsupported expert parameters in the solver. However, the improvement is small and the effects on other parts of the flow is unknown.

Consequently, these options are not employed for production-runs and the remainder of this work presents results obtained with the pressure-based solver and the bounded second order Euler scheme.

7. Investigation of Operating Envelope

In his experiments Lungu varied the distance between resonator and injector in order to determine the best s/d ratio, where the highest gas temperatures are achieved. He observed, that outside a certain s/d-range no resonance and no temperature increase occurred. In this section these experiments are reproduced numerically. Since wall temperatures are not necessarily needed to establish the s/d range, at which strong oscillations occur, the domain incorporating the thin-wall modes is used.

In this section transient results are presented with respect to

$$\vartheta = \frac{t}{\tau_{conv}} \tag{7}$$

which approximates the time in number of flow cycles since the start of the simulation.

Due to the relatively large ratio of injector to outlet throat cross section area the igniter pressure approaches its design value rather slowly, in the order of 20-40 flow cycles. However, for the current evaluation only the quasi-steady limit cycle, at which the igniter is operated under nominal conditions, is of interest. Therefore, the transient simulations are initialized from a steady-state calculation. But due to the inherently unstable nature of the problem, a converged steady solution can usually not be obtained. Consequently, slight variations in the initial conditions of different load points occur. But as the left part of Figure 10 shows, disturbances from the initial conditions are quickly dampened away and a gradual transition to the quasi-steady limit cycle occurs within about $10\tau_{conv}$. Evaluation of the limit cycle therefore only takes data from $t \geq 10\tau_{conv}$ into account.

It should be noted, that the thin-wall model lacks the thermal low-pass properties of an actual, solid wall. Therefore, time-domain temperature signals like the one shown in Figure 10 are subjected to a sliding average filter with a width of $2\tau_{conv}$ in order to smooth out short variations and highlight the general trends over larger timescales.

The right part of Figure 10 shows the pressure-RMS at the tip of the cavity for various s/d ratios and turbulence Clipping Factors. It can be seen, that the value of the Clipping Factor strongly affects the pressure oscillations. This

DOI: 10.13009/EUCASS2019-360

demonstrates, that C_{lim} and turbulence in general plays an important role in the prediction of the oscillation mode of the resonator, which is in strong contrast to the findings of Lee et al who claim, that the effects of turbulence are negligible for this type of flow [34]. The reason for this strong sensitivity is still under investigation, but it is likely that this parameter merely affects the pressure distribution of the free jet.

Figure 10 (right) also includes is the temperature increase observed in the experiments on the secondary y-axis. It can be seen, that for a Clipping Factor of 10 the tip RMS pressure qualitatively follows the same trend as the temperatures measured in the experiment but fails to reproduce the sudden switch in operating mode around s/d=3. Instead, around s/d=3 the RMS pressure falls rather gradually. Which seems to suggest that the selected schemes can qualitatively reproduce the operating mode if a suitable value for C_{lim} is selected, but that not all effects are resolved sufficiently well.

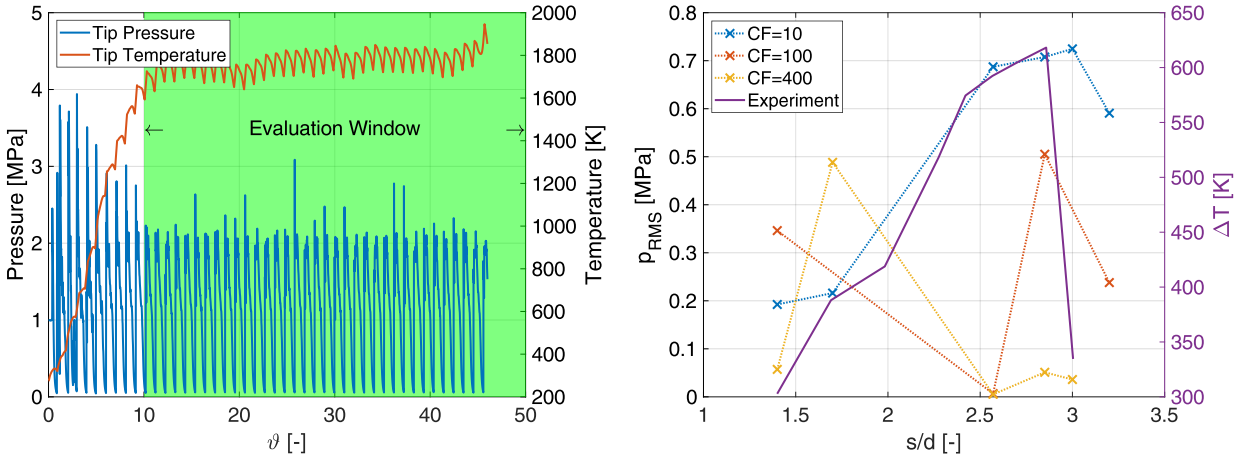

Figure 10: Left: Pressure and temperature traces for resonating cases at tip of resonator and the window, over which results are evaluated. Right: comparison of simulated RMS pressure at resonator tip with experimental temperature increase.

Figure 11 shows a more detailed comparison between the dynamic pressure data of both experiment and simulation at s/d=2.85. The experimental pressure data was sampled with 50 kHz at the igniter wall outside of the resonator and is only available as an uncalibrated voltage signal. In contrast, the pressure signal from the simulation is sampled directly at the closed cavity wall at 500 kHz and is thus not superimposed by reflections and other disturbing flow features. However, since the data cannot be compared quantitatively, both spectra are normalized with respect to the largest peaks.

It can be seen, that the position of the primary peak closest to the fundamental frequency is reproduced remarkably well, which suggests, that the large-scale flow features are captured with sufficient accuracy. The simulation also captures multiple higher harmonics, where the magnitude drops with higher order, which disagrees with experimental results, where the magnitude of the harmonics seems to increase with increasing order.

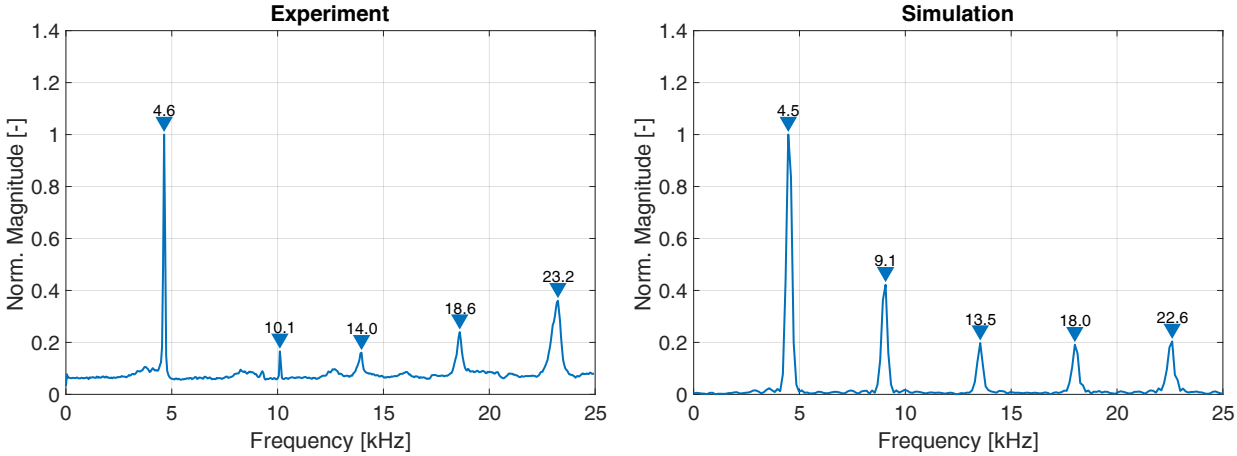

Figure 11: Comparison of normalized pressure magnitudes obtained from dynamic pressure sensor in experiment and simulated pressure probe in resonator cavity.

DOI: 10.13009/EUCASS2019-360

However, the small peak at 10.1 kHz may be an artefact in the experimental data, since it does not seem to be a higher harmonic. These differences require further analysis with additional sample points which is currently beyond the scope of this work.

8. Transient Heat-up and Energy Balance

With the thin-wall model, a direct comparison between experimental and numerical heating rates is not possible, since it lacks some effects required for accounting for all heat losses. For this reason, a single configuration with s/d=2.71 was also simulated incorporating solid and deadwater zones, which provides a wealth of additional data. Most importantly, it allows tracking heat losses by establishing the energy balance over various control volumes, which reduce the maximum fluid temperature and increase the time to reach quasi-steady operation.

To get a first impression, Figure 12 (left) compares the transient, experimentally determined resonator temperature at the tip with the simulated value. It should be noted, that the numerical data is plotted over the solid-time. It can be seen, that the immediate start-up transient differs considerably between numerics and experiment. This can partly be attributed to the response time of the supply system, which is estimated from the pressure measured in the igniter chamber to be $\approx 250ms$. Since the transient simulation is initialized from a steady-state solution which skips this run-in phase, the results were shifted accordingly. Obviously more simulation time is needed to determine, if the otherwise good agreement continues over the entire experiment duration.

However, even the rather short simulation provides interesting insights, since the flow reaches convective near-steady conditions after ≈ 10 flow cycles. This can be seen in the right part of Figure 12, which shows the total, integrated heat flux through the walls enclosing the cavity fluid, as well as the total, mass-integrated enthalpy of the fluid itself. After a short run-in phase of 10 cycles the fluid enthalpy remains nearly constant and only increases slowly with a rate below 1 W. In contrast, the total wall heat flux is considerably larger with a mean value of ≈25 W. The sum of both can be considered the thermal power of the resonant heating process.

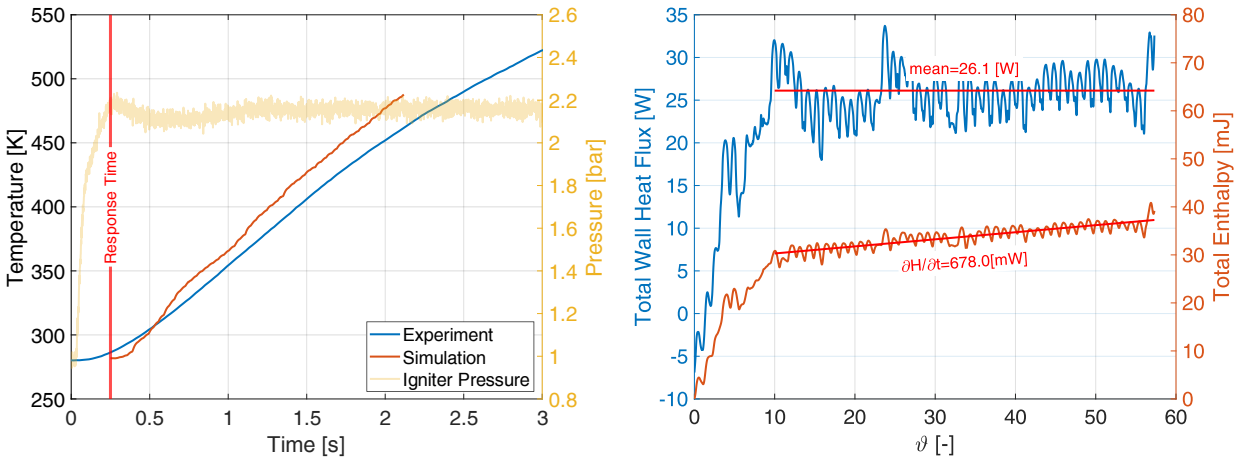

Figure 12: Left: Comparison of experimental and simulated tip temperatures. Right: Total wall heat flux through the hot side of the resonator walls and the total enthalpy of the cavity fluid over non-dimensional time.

It is clear, that most of the thermal power is used for slowly increasing the temperature of the solid, rather than raising the fluid temperature. Consequently, the solid timescales also set the thermal timescales of the fluid.

If future developments desire to reduce the necessary igniter pre-heating times, increasing the overall thermal power by using higher supply pressures or different fluids is an obvious option. Attempts to reduce the timescales of the solid by using either low-α materials or by using thinner walls may also provide the desired effects, but the choice of materials is strongly limited by the required oxidation resistance at high temperatures. However, reducing the thermal contact between fluid and solid may be the most efficient approach, but most likely requires completely new cavity geometries.

A closer look at the deadwater region between the inner resonator solid and the protective cap suggests another easy to implement improvement. Even though the dual-choke design of the ignitor maintains a constant average NPR, the strong oscillations in the resonance cavity also lead to small instantaneous variations in NPR. As can be seen in Figure 13, these are enough to create a small jet which repeatedly impinges on the hot outer wall of the resonator, leading to increased convective heat transfer. Since a considerable portion of this fluid is expulsed again during the outflow phase, the transferred heat is lost to the resonant heat-up process. This can easily be avoided by minor changes in geometry and should be evaluated during the next test series.

DOI: 10.13009/EUCASS2019-360

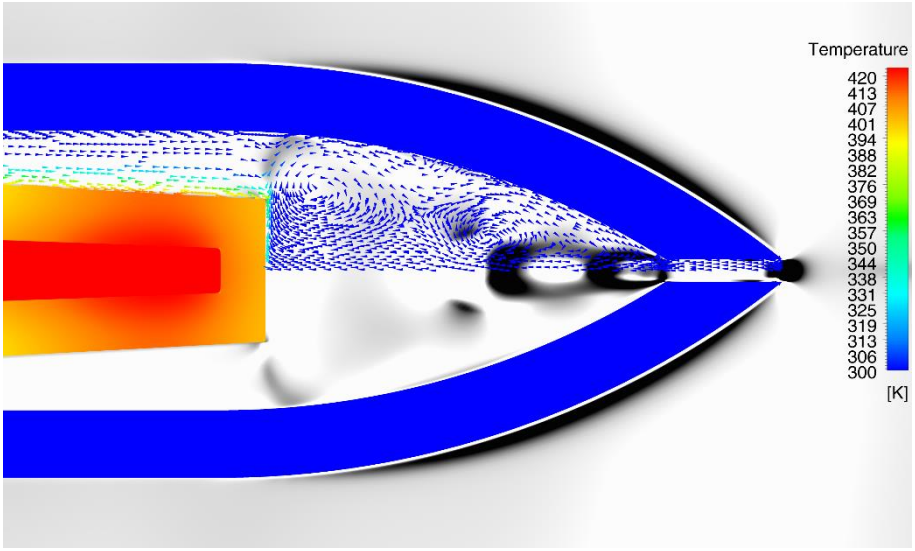

Figure 13: Detailed view of the deadwater region between the inner resonator solid and the protective cap.

9. Conclusions

In the presented study a resonance ignition system with conical resonator cavity and a single propellant injector was simulated with the Ansys Fluent solver. While the density-based form of the solver provides superior shock resolution and reduced mesh and timestep sensitivity, it also experiences stability issues which prohibit its use for production-run type of problems. Consequently, results for the highly transient resonant heat up were obtained with the pressure-based scheme. However, a re-evaluation of the density-based solver should be conducted in future releases of the software.

All calculations presented in this work were performed on a 2D axisymmetric domain on a fully conformal hex mesh. A mesh study utilizing a least-squares version of the Grid Convergence Index algorithm shows, that results are remarkable insensitive to mesh resolution and that the chosen mesh is sufficient to reproduce the relevant flow features. Sensitivity to timestep size was found to be even lower.

A parametric study using the thin-wall model to simplify thermal wall boundary conditions shows, that the s/d range, in which strong oscillations occur, is sensitive to the degree in which turbulence production limiting occurs. This suggests, that more work on the validation and fine-tuning of suitable turbulence models is necessary. The observed sensitivity may also suggest, that the Boussinesq assumption does not hold for Hartmann-Sprenger type of flows or that 3D effects may be of importance. While earlier studies that investigated 3D effects in a cylindrical resonator cavity were inconclusive, simulation results incorporating scale resolving turbulence models seemed promising [35]. However, with a suitable choice for the turbulence production limiter good qualitative agreement between experiment and simulation regarding the operating range could be achieved, but more work is required to reproduce the sudden switch in operating mode at higher s/d ratios. This nevertheless makes the simplified wall model a candidate for use in early design phases. However, due to the simplified thermal wall boundary conditions resonant gas temperatures cannot be directly compared to experimental values.

For more accurately reproducing the transient thermal behavior during resonant heating the solid resonator material and a small deadwater region at the tip of the resonator are included in simulations investigating a selected s/d ratio. By applying different timesteps in fluid and solid zones the computational effort for covering the complete experiment duration is greatly reduced. These simulations allow a direct comparison of measured and simulated data for both temperatures and pressures. It is shown, that most of the thermal power generated by the resonant heating process is lost to the resonator walls. The presented simulations suggest, that igniter performance can be improved by further reducing the energy exchange between the gas in the resonator cavity and the resonator itself, as well as between the solid resonator material and the enclosed deadwater region.

10. Acknowledgements

The authors gratefully acknowledge the Gauss Centre for Supercomputing e.V. (GCS, www.gauss-centre.eu) for funding this project by providing computing time on the GCS supercomputer SuperMUC at Leibniz Supercomputing Centre (LRZ, www.lrz.de). Thanks are also due for the continuous support from Munich Aerospace e. V.

DOI: 10.13009/EUCASS2019-360

11. References

[1] B. Nufer, “A Summary of NASA and USAF Hypergolic Propellant Related Spills and Fires,” in *SpaceOps 2010 Conference*, Alabama, 2010.

[2] E. Schlosser, Command and Control: Nuclear Weapons, the Damascus Accident, and the Illusion of Safety., Penguin Press, 2013.

[3] E. Musk, “Twitter,” 30 11 2013. [Online]. Available: https://twitter.com/elonmusk/status/406806983023820800.

[4] Ariane Group, „Aerospace Propulsion Products Space Activities,“ [Online]. Available: https://app.ariane.group/en/our-activities/space-activities/.

[5] G. Frenken, E. Vermeulen, F. Bouquet and B. Sanders, “Development Status of the Ignition System for Vinci,” in *38th AIAA/ASME/SAE/ASEE Joint Propulsion Conference & Exhibit*, Indianapolis, 2002.

[6] E. Musk, “Twitter,” 12 2 2018. [Online]. Available: https://twitter.com/elonmusk/status/963107229523038211.

[7] J. Hartmann, “On a New Method for the Generation of Sound Waves,” *Physics Review,* no. 20, 1922.

[8] J. Hartmann und B. Trolle, „New Investigation on the Air Jet Generator for Acoustic Waves,“ 1926.

[9] H. Sprenger, „Über thermische Effekte in Resonanzrohren,“ *Mitteilungen aus dem Institut für Aerodynamik an der ETH Zürich,* 1954.

[10] V. Sarohia und L. Back, „Experimental Investigation of Flow and Heating in a Resonance Tube,“ *J. Fluid Mech.,* Nr. 94, 1979.

[11] C. Bauer und O. Haidn, „Design and Test of a Resonance Ignition System for Green In-Orbit Propulsion Systems,“ in *52nd AIAA/SAE/ASEE Joint Propulsion Conference*, Salt Lake City, 2016.

[12] S. Murugappan and E. Gutmark, “Parametric study of the Hartmann-Sprenger tube,” *Experiments in Fluids,* vol. 38, 2005.

[13] P. Lungu, C. Bauer and O.-J. Haidn, “Operational behaviour investigation of Hartmann-Sprenger Tube based resonance ignition systems for oxygen/methane in-orbit propulsion applications,” in *Space Propulsion Conference*, 2018.

[14] P. Lungu, C. Bauer and O.-J. Haidn, "Design aspects and characterisation of a resonance igniter for oxygen/methane in-orbit propulsion systems," in *8th European Conference for Aeronautics and Space Sciences (EUCASS)*, Madrid, 2019.

[15] B. Leonard and S. Mokhtari, “ULTRA-SHARP Nonoscillatory Convection Schemes for High-Speed Steady Multidimensional Flow,” 1990.

[16] SAS IP Inc., “Fluent Theory Guide, v182”.

[17] V. Venkatakrishnan, “Convergence to Steady State Solutions of the Euler Equations on Unstructured Grids with Limiters,” *Journal of Computational Physics,* vol. 118, pp. 120-130, 1995.

[18] Z. Wang, “A fast nested multi-grid viscous flow solver for adaptive Cartesian/Quad grids,” in *AIAA Fluid Dynamics Conference*, New Orleans, LA, 1996.

[19] C. Rhie and W. Chow, “Numerical Study of the Turbulent Flow Past an Airfoil with Trailing Edge Separation,” *AIAA Journal,* vol. 21, no. 11, pp. 1525-1532, 1983.

[20] T. Shih, W. Liou, A. Shabbir, Z. Yang and J. Zhu, "A New k-e Eddy Viscosity Model for High Reynolds Number Turbulent Flows - Model Development and Validation," 1994.

[21] F. Menter, "Zonal Two Equation k-w Turbulence Models for Aerodynamic Flows," in *24th Fluid Dynamics Conference*, Orlando, 1993.

[22] F. Menter, "Two-Equation Eddy-Viscosity Turbulence Models for Engineering Applications," *AIAA Journal,* vol. 32, no. 8, p. 1598ff., August 1994.

[23] E. Wolf, Nanophysics and Nanotechnology, 2nd ed., 2008.

[24] E. Marin, “Characteristic dimensions for heat transfer,” *Lat. Am. J. Phys. Educ.*, vol. 4, no. 1, pp. 56-60, 2010.

[25] EOS GmbH, “Material data sheet EOS CobaltChrome MP1,” 2011.

[26] Acnis Group, "acnis-titanium.com," [Online]. Available: http://www.acnis-titanium.com/wp-content/uploads/2017/10/CO-Cr-MOforge_FT029-UK.pdf.

[27] CarTech, „CarTech Micro-Melt BioDur CCM Alloy,“ [Online]. Available: http://cartech.ides.com/datasheet.aspx?i=101&E=334.

DOI: 10.13009/EUCASS2019-360

[28] H. Kuttruff, Acoustics: An Introduction, CRC Press, 2007.

[29] Y. J. Zhang, Z. H. Huang and L. J. Wei, “Experimental and kinetic study on ignition delay times of methane/hydrogen/oxygen/nitrogen mixtures by shock tube.,” *Chinese Sci Bull*, vol. 56, pp. 2853-2861, 2011.

[30] Verein Deutscher Ingenieure, „Fa 4,“ in *VDI Wärmeatlas*, 2006.

[31] G. Greene, C. Finfrock and T. Irvine Jr, “Total hemispherical emissivity of oxidized Inconel 718 in the temperature range 300-1000°C,” *Experimental Thermal and Fluid Science*, vol. 22, pp. 145-153, 2000.

[32] I. Celik, U. Ghia, P. Roache, C. Freitas, H. Coleman and P. Raad, "Procedure for Estimation and Reporting of Uncertainty Due to Discretization in CFD Applications," *Journal of Fluids Engineering*, vol. 130, July 2008.

[33] L. Eca and M. Hoekstra, "Discretization Uncertainty Estimation based on a Least Squares version of the Grid Convergence Index," in *2nd Workshop on CFD Uncertainty Analysis*, Lisbon, 2006.

[34] J. Lee, D. Lim, S. Seo and S. Kang, “Numerical analysis of the thermal characteristics of a gas-dynamic ignition system,” *Journal of Mechanical Science and Technology*, vol. 32, no. 5, pp. 2385-2390, 2018.

[35] Bauer and Haidn, “Numerical Investigation of 3D Effects in Hartmann-Sprenger-Tubes,” in *EUCASS*, 2015.